Parker Solar Probe Observations of High Plasma β Solar Wind from the Streamer Belt

Jia Huang[1], J. C. Kasper[2,3], Davin E. Larson[1], Michael D. McManus[1], P. Whittlesey[1], Roberto Livi[1], Ali Rahmati[1], Orlando Romeo[1], K. G. Klein[4], Weijie Sun[3], Bart van der Holst[3], Zhenguang Huang[3], Lan K. Jian[5], Adam Szabo[5], J. L. Verniero[5], C. H. K. Chen[6], B. Lavraud[7], Mingzhe Liu[8], Samuel T. Badman[9], Tatiana Niembro[9], Kristoff Paulson[9], M. Stevens[9], A. W. Case[9], Marc Pulupa[1], Stuart D. Bale[1,6,10,11], and J. S. Halekas[12]

[1] Space Sciences Laboratory, University of California, Berkeley, CA 94720, USA; huangjia.sky@gmail.com
[2] BWX Technologies, Inc., Washington, DC 20001, USA
[3] Climate and Space Sciences and Engineering, University of Michigan, Ann Arbor, MI 48109, USA
[4] Lunar and Planetary Laboratory, University of Arizona, Tucson, AZ 85719, USA
[5] Heliophysics Science Division, NASA Goddard Space Flight Center, Greenbelt, MD 20771, USA
[6] School of Physics and Astronomy, Queen Mary University of London, London E1 4NS, UK
[7] Institut de Recherche en Astrophysique et Planétologie, CNRS, UPS, CNES, Université de Toulouse, Toulouse, France
[8] LESIA, Observatoire de Paris, Université PSL, CNRS, Sorbonne Université, Université de Paris, 5 place Jules Janssen, F-92195 Meudon, France
[9] Smithsonian Astrophysical Observatory, Cambridge, MA 02138 USA
[10] Physics Department, University of California, Berkeley, CA 94720-7300, USA
[11] The Blackett Laboratory, Imperial College London, London, SW7 2AZ, UK
[12] Department of Physics and Astronomy, University of Iowa, Iowa City, IA 52242, USA

Abstract

In general, slow solar wind from the streamer belt forms a high plasma β equatorial plasma sheet around the heliospheric current sheet (HCS) crossing, namely, the heliospheric plasma sheet (HPS). Current Parker Solar Probe (PSP) observations show that the HCS crossings near the Sun could be full or partial current sheet (PCS) crossings, and they share some common features but also have different properties. In this work, using the PSP observations from encounters 4–10, we identify streamer belt solar wind from enhancements in plasma β, and we further use electron pitch angle distributions to separate it into HPS solar wind around the full HCS crossings and PCS solar wind in the vicinity of PCS crossings. Based on our analysis, we find that the PCS solar wind has different characteristics as compared with HPS solar wind: (a) the PCS solar wind could be non-pressure-balanced structures rather than magnetic holes, and the total pressure enhancement mainly results from the less reduced magnetic pressure; (b) some of the PCS solar wind is mirror-unstable; and (c) the PCS solar wind is dominated by very low helium abundance but varied alpha–proton differential speed. We suggest that the PCS solar wind could originate from coronal loops deep inside the streamer belt, and it is pristine solar wind that still actively interacts with ambient solar wind; thus, it is valuable for further investigations of the heating and acceleration of slow solar wind.

Unified Astronomy Thesaurus concepts: Slow solar wind (1873); Interplanetary magnetic fields (824); Space plasmas (1544)

1. Introduction

The Parker Solar Probe (PSP) aims to enter the atmosphere of the Sun and provide in situ measurements to uncover the properties of solar wind close to its source regions (Fox et al. 2016). The PSP had completed its initial 14 orbits by 2022 December, with the deepest perihelion reaching a heliocentric distance of about 13.3 solar radii (R_S), and it entered the solar corona for the first time on 2021 April 28 (Kasper et al. 2021). The PSP has many extraordinary observations, and the new data give us a chance to investigate the properties of the streamer belt solar wind near the Sun.

The origin and evolution of the slow solar wind are still debatable, and its multiple source regions are one of the difficulties. The streamer belt is believed to be a certain source of the slow solar wind; thus, it is suitable to study the nature of the slow solar wind from a specific source region with less uncertainty. Solar wind from the streamer belt generally forms a low-speed but high plasma β solar stream region, i.e., a heliospheric plasma sheet

(HPS), which always embeds a heliospheric current sheet (HCS; e.g., Borrini et al. 1981; Winterhalter et al. 1994; Smith 2001; Crooker et al. 2004; Suess et al. 2009; Liu et al. 2014; Huang et al. 2016a). However, current PSP observations reveal that HCS crossings and HPS solar winds in the near-Sun environment are much more dynamic than those at 1 au; for example, the HCSs have multiple crossings (Lavraud et al. 2020; Phan et al. 2020; Szabo et al. 2020), the magnetic reconnections are prevalent around the HCS crossings (Lavraud et al. 2020; Phan et al. 2020, 2021), and multiple small-scale structures are found in HPS solar winds (Lavraud et al. 2020; Rouillard et al. 2020; Szabo et al. 2020; Zhao et al. 2021; Réville et al. 2022).

Moreover, Lavraud et al. (2020) and Phan et al. (2021) found that there is a category of partial current sheet (PCS) crossings, which are different from the well-known HCS crossings defined as full crossings of two magnetic field sectors with different polarities. The PCS crossings stay at the same magnetic field sector without crossing the sector boundary. They generally appear in the vicinity of HCS crossings and also show signatures of density enhancement, but they exhibit more significant changes in suprathermal electrons and have smaller magnetic field rotation as compared with HCS crossings, and sometimes they display reconnection jet signatures (Lavraud et al. 2020; Phan et al. 2021).

The PCS crossings could be caused by the warped HCSs (e.g., Peng et al. 2019), but their signatures of long duration and recurrent appearance imply that they are most likely generated by the traveling large plasma blobs bulging onto both sides of the HCS crossings (e.g., Phan et al. 2004; Lavraud et al. 2020; Phan et al. 2021). As a result, the PCS crossings represent the pristine state of the solar wind from the streamer belt, and it is valuable to compare the PCS solar wind with the HCS solar wind (i.e., HPS) to infer their differences in kinetic properties and origins.

In this work, we identify the HPS and PCS solar wind from encounter 4 to encounter 10 (E4–E10), and we then compare their pressures, temperature anisotropies, and helium signatures to infer their different behaviors and origins. In Section 2, we introduce the data we used in this work. Section 3 presents the results in E4, whereas Section 4 shows the multi-event analysis from E4 to E10. The discussion and summary are included in Sections 5 and 6, respectively.

2. Data

The instrument suites of Solar Wind Electrons, Alphas, and Protons (SWEAP; Kasper et al. 2016) and FIELDS (Bale et al. 2016) on board PSP provide the data used in this work. SWEAP includes the Solar Probe Cup (SPC; Case et al. 2020), Solar Probe Analyzer for Electrons (SPAN-E; Whittlesey et al. 2020), and Solar Probe Analyzer for Ions (SPAN-I; Livi et al. 2022). SWEAP is designed to measure the velocity distributions of solar wind electrons, alpha particles, and protons (Kasper et al. 2016). FIELDS is designed to measure DC and fluctuation magnetic and electric fields, plasma wave spectra and polarization properties, the spacecraft floating potential, and solar radio emissions (Bale et al. 2016).

In this work, we use the electron data from SPAN-E and the magnetic field data from FIELDS. The electron density is derived from the analysis of the plasma quasi-thermal noise (QTN) spectrum measured by the FIELDS Radio Frequency Spectrometer (Pulupa et al. 2017; Moncuquet et al. 2020). The fitted proton and alpha data from SPAN-I are used to study the alpha-associated signatures. We also select the best SPAN-I and SPC data to calculate the radial power-law indices of the pressures, as shown in Appendix B. The temperature components are retrieved from bi-Maxwellian fitting to the proton channel spectra observed by SPAN-I. SPAN-I measures the three-dimensional velocity distribution functions of the ambient ions in the energy range from several eV/q to 20 keV/q with a maximum time resolution of 0.437 s, and it has a time-of-flight section that enables it to differentiate the ion species (Kasper et al. 2016). The details of the fitted proton and alpha data are described in Finley et al. (2020), Livi et al. (2022), and McManus et al. (2022). However, the SPAN-I measurements used here are from low-cadence downlinked data, and the cadences of the fitted proton and alpha data are 6.99 and 13.98 s, respectively (Finley et al. 2020; Verniero et al. 2020; McManus et al. 2022). The FIELDS instrument collects high-resolution vector magnetic fields with variable time resolutions. The four samples per cycle (i.e., four samples per 0.874 s) data are used here.

3. E4 Results

3.1. Overview of High Plasma β Solar Wind in E4

Figure 1 presents an overview of high plasma β solar wind in E4 between 2020 January 30 12:00 UT and 2020 February 2

00:00 UT. From top to bottom, the panels show plasma β, QTN electron number density Ne and solar wind speed Vp, proton temperatures (total temperature Tp, parallel temperature $T_{\parallel p}$, and perpendicular temperature $T_{\perp p}$), magnetic field components in RTN coordinates, radial magnetic field to total magnetic field strength ratio Br/|B|, normalized pitch angle distribution of suprathermal electrons (e-PAD) at energy of 346.5 eV, angular distance to the HCS crossing ϕ_{HCS} (degrees), alpha-to-proton abundance ratio Na/Np, and alpha–proton differential speed normalized by local Alfvén speed $\Delta Vap/V_A$. The three shaded regions mark the high-β solar winds, with the blue dashed lines indicating the middle times of switchbacks identified with our algorithm (Kasper et al. 2019; Huang et al. 2023). Here $\beta = 2\mu_0\, n_p\, k_B\, T_p/B^2$, where μ_0 is the vacuum magnetic permeability, k_B is the Boltzmann constant, B is the magnetic field strength, and n_p and T_p are the number density and temperature of protons, respectively. The red dashed vertical line in region 3 suggests the HCS crossing, when the Br/|B| changes polarity (panel (e)) and the e-PAD changes direction (panel (f)) simultaneously.

In this work, we use high β, which is larger than 1 and also larger than that in the ambient solar wind, as the primary signature to identify the streamer belt solar wind. We keep using the HPS solar wind to name the solar wind in the vicinity of full HCS crossings, whereas we define the solar wind around PCS crossings as the PCS solar wind. As stated in the Introduction, we further combine the magnetic field polarity and e-PAD to indicate full HCS or PCS crossings; i.e., the magnetic field polarity and e-PAD both change directions before and after full HCS crossings, whereas the magnetic field polarity does not change, but the e-PAD is significantly scattered around PCS crossings. Generally, we search for PCS crossings about 2 days before and after HCS crossings. Therefore, regions 1 and 2 are PCS solar wind, and region 3 is HPS solar wind, which is consistent with the classification in Phan et al. (2021). The solar wind speed is less than 300 km s^{-1} during this time period, and it does not change a lot inside and outside the three regions. The e-PAD in panel (f) changes direction in the HPS solar wind, but it stays predominantly in the same direction and scatters a lot in the PCS solar wind, inferring that complicated physical processes may be involved (Halekas et al. 2021). We note that the HPS solar wind is slightly closer to the HCS crossing than the PCS solar wind, as indicated by the angular distance to the HCS crossing ϕ_{HCS} derived from the potential-field source-surface model (Badman et al. 2020; Stansby et al. 2020; Szabo et al. 2020; Chen et al. 2021a). In these regions, we can see that the Ne and temperatures increase significantly, but the magnetic field strength |B| decreases greatly at the same time; thus, the β enhances profoundly as compared with the ambient solar wind, and sometimes it can even reach about 1000. Some of the super-high-β solar wind involves the switchbacks, as shown by the blue dashed lines, due to the magnetic field reversals leading to very small magnetic pressures. However, there is still some super-high-β solar wind that shows no relation to the switchbacks, and this kind of solar wind seems to have low Na/Np, implying that the solar streams should come from the coronal loops deep inside the streamer belt (Suess et al. 2009). Moreover, in the HPS and PCS solar winds, $T_{\parallel p}$ and $T_{\perp p}$ also increase, implying that their thermal states may not be stable, and the $\Delta Vap/V_A$ deviates from zero, indicating that the solar wind may still be under evolution.

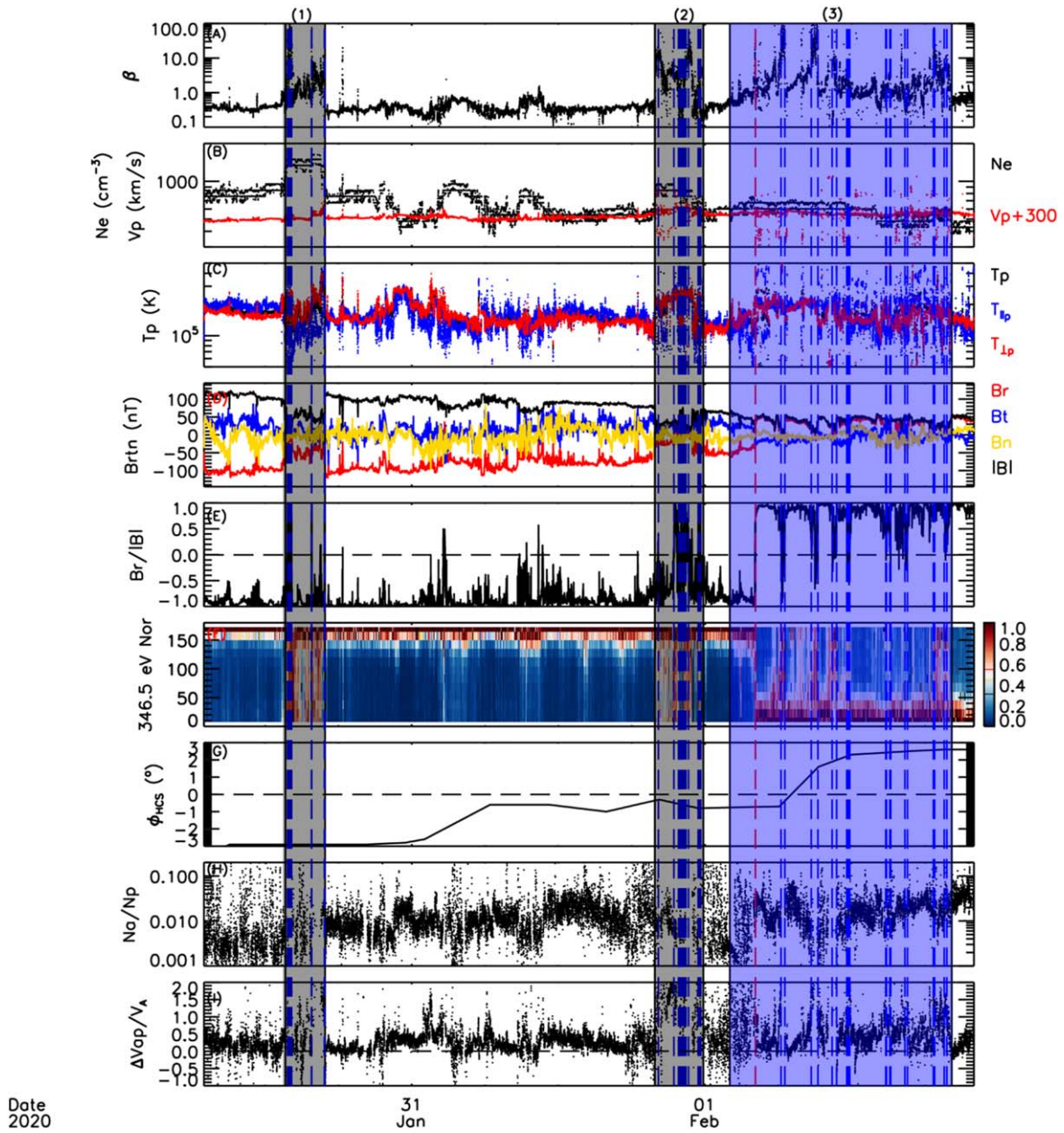**Figure 1.** Overview of the high plasma β streamer belt solar wind in E4. From top to bottom, the panels show plasma β, electron number density Ne and solar wind speed Vp, proton temperatures, magnetic field components in RTN coordinates, radial magnetic field to total magnetic field strength ratio Br/|B|, normalized e-PAD at energy of 346.5 eV, angular distance to the HCS crossing ϕ_{HCS} (degrees), alpha-to-proton abundance ratio Na/Np, and alpha–proton differential speed normalized by local Alfvén speed $\Delta Vap/V_A$. In panel (b), we add 300 km s^{-1} to the solar wind speed. In panel (c), the perpendicular temperature ($T_{\perp p}$), parallel temperature ($T_{\parallel p}$), and total temperature (T_p) are indicated by red, blue, and black dots, respectively. Gray shaded regions 1 and 2 mark high plasma β solar winds around PCS crossings. The blue shaded region 3 is the HPS solar wind around the HCS crossing, as indicated by the red vertical dashed line. The blue vertical dashed lines represent the switchbacks in these high-β solar winds.

3.2. Pressure Variations

Thermal pressure gradients drive the solar wind flow out from the solar corona (Cranmer & Cranmer 2019; Owens 2020). In general, pressure-balanced structures are normal in interplanetary space, such as tangential discontinuities, rotational discontinuities, magnetic holes, small transients, magnetic reconnection exhausts, and so on (Belcher et al. 1969; Belcher & Davis 1971; Burlaga 1971; Burlaga et al. 1990; Wei et al. 2006; Stevens & Kasper 2007; Yu et al. 2014; Mistry et al. 2017). Moreover, the total pressure of the HPS is comparable to that in the ambient solar wind, and the small-scale structures inside HPSs also show a pressure-balanced

signature (Burlaga et al. 1990; Winterhalter et al. 1994; Crooker et al. 2004; Yamada et al. 2010; Foullon et al. 2011; Yu et al. 2014). However, non-pressure-balanced structures are rare in the interplanetary medium, except for large magnetic clouds in expansions and the corotating interaction regions that are formed by compressions. In addition, interplanetary shock fronts and magnetic cloud boundary layers are also found to be non-pressure-balanced (Wei et al. 2006; Zuo et al. 2006; Wang et al. 2010; Priest 2014; Zhou et al. 2018, 2019). The interplanetary shock front is a relatively thin transitional layer from the quasi-uniform solar wind to the disturbed solar wind, and the interactions within the shock front are efficient to

convert the flow energy into thermal energy and accelerate particles to significant energies (e.g., Priest 2014; Sapunova et al. 2017). The boundary layers of the magnetic clouds are formed as the magnetic clouds interact with ambient solar wind during propagation, and they have complicated fine structures like slow shock, magnetic reconnection exhaust, magnetic field reversal, and enhanced wave activity, implying that the boundary layer is sufficient to heat and accelerate the encountered solar wind (Wei et al. 2003, 2006; Zuo et al. 2006; Wang et al. 2010; Priest 2014; Zhou et al. 2018, 2019). Therefore, pressure is an important indicator of solar wind states, and a non-pressure-balanced signature is always associated with crucial physical processes like plasma heating and acceleration, plasma wave activity, and magnetic reconnections. As PSP dives into the solar atmosphere, it has chances to observe more pristine solar winds that still actively interact with the ambient solar wind. Consequently, it is essential to investigate the pressure variations in the streamer belt solar wind in the inner heliosphere, which may shed light on the long-standing mysteries of the slow solar wind in terms of the formation, evolution, heating, and acceleration processes.

Figure 2 shows the pressure variations in the E4 streamer belt solar wind. From top to bottom, the panels show the normalized e-PAD at energy of 346.5 eV, total pressure (P_{total}) and expected total pressure (P_{expt}), pressure components (P_B, P_e, and P_{p+a}), normalized total pressure (P_{total} Nor), and normalized pressure components. The three shaded regions mark the high-β streamer belt solar wind as in Figure 1. The definitions of magnetic pressure P_B, electron pressure P_e, proton and alpha pressure P_{p+a}, and total pressure P_{total} are presented in Appendix A. Since the pressures vary with heliocentric distances, and PSP has an elliptical orbit, we investigate their radial evolution in Appendix B. We further use the derived functions to normalize the pressures to 20 R_S as shown in panels (d) and (e) and estimate the expected total pressure as a function of radial distance $P_{expt} = 10^{5.96} \times R^{-3.31}$ (nPa) in panel (b), where R is the heliocentric distance in units of R_S. From panel (b), we can see that P_{total} changes about threefold in about 2 days, indicating that it is necessary to normalize the pressures when studying pressure-associated signatures.

In the high-β streamer belt solar wind, we can see that the total pressure enhances as compared with the ambient solar wind. The enhancements can be seen both from the P_{total} Nor in panel (d) and from the comparison between P_{total} and P_{expt} in panel (b). In the PCS solar wind, the P_{total} Nor increases by about 15% and 25% in regions 1 and 2, respectively. In panel (e), we can see that the magnetic pressure decreases significantly in the PCS solar wind, whereas the thermal pressure increases more profoundly, resulting in the enhancement of total pressure. In addition, we note that the total pressure also shows signatures of enhancement in the HPS solar wind, with the variations of the pressure components similar to those in the PCS solar wind. This implies that the HPS solar wind in the inner heliosphere may be more active than that observed at 1 au and beyond. However, our results in Section 4.1 indicate that the pressure enhancements are much more distinctive in the PCS solar wind than in the HPS solar wind, indicating that the PCS solar wind could be a non-pressure-balanced structure. This characteristic suggests that

the PCS solar wind in the inner heliosphere could be pristine solar wind that still actively interacts with ambient solar wind.

Besides, we can see that the switchbacks, as marked by blue dashed lines, could modify the total pressure; i.e., the crash of the magnetic pressure leads to the temporary decrease of the total pressure inside the streamer belt solar wind. But the total pressure of the switchbacks seems to be comparable to the ambient solar wind outside the high plasma β solar wind, implying that the switchbacks are roughly pressure-balanced structures, as suggested by Bale et al. (2021).

3.3. Temperature Anisotropy Characteristics

The thermodynamic property is pivotal to understanding the kinetic processes governing the dynamics of the interplanetary medium (Kasper et al. 2002, 2003; He et al. 2013; Maruca & Kasper 2013; Huang et al. 2020b). Temperature anisotropy ($T_{\perp p}/T_{\parallel p}$) arises when $T_{\perp p}$ and/or $T_{\parallel p}$ departs from thermal equilibrium, which indicates that anisotropic heating and/or cooling processes act preferentially in one direction (Maruca et al. 2011), and such preferential heating/cooling is supported by the observed departures of $T_{\perp p}/T_{\parallel p}$ from adiabatic predictions in solar wind observations (Gary 1993; Matteini et al. 2007). As the temperature anisotropy departs from unity, anisotropy-driven instabilities such as mirror, ion–cyclotron, and parallel and oblique firehose instabilities arise and act to isotropize the plasma (Gary 1993; Maruca et al. 2011). Therefore, a study of the temperature anisotropy characteristics in the PCS and HPS solar wind is helpful to differentiate the dynamic processes therein.

Figure 3 shows the characteristics of the temperature anisotropies in the E4 streamer belt solar wind. Panels (a) and (c) display the $T_{\perp p}/T_{\parallel p}$ signatures in the HPS solar wind, whereas panels (b) and (d) show the same parameters in the PCS solar wind. Panels (a) and (b) present the occurrence rates of temperature anisotropies in the HPS and PCS solar winds, respectively. Panels (c) and (d) exhibit the $T_{\perp p}/T_{\parallel p}$ versus parallel plasma β ($\beta_{\parallel p}$) in the HPS and PCS solar winds, respectively. The colored dashed lines are instabilities, as indicated by the legend, with thresholds from Hellinger et al. (2006), and the black line is the anticorrelation relationship between $T_{\perp p}/T_{\parallel p}$ and $\beta_{\parallel p}$ derived by Marsch et al. (2004).

In the HPS solar wind, we can see that the $T_{\perp p}/T_{\parallel p}$ is almost isotropic (~1) from panel (a), and the $T_{\perp p}/T_{\parallel p}$ versus $\beta_{\parallel p}$ distribution is well limited by the instabilities, as indicated in panel (c). These signatures suggest that the HPS solar wind is generally in a thermal equilibrium state. However, the PCS solar wind shows different signatures. On one hand, the PCS solar wind seems to have two populations, as shown by the right panels. One population has isotropic temperature anisotropy, whereas the other population is much more anisotropic. On the other hand, the isotropic population is well limited by the instabilities, but part of the anisotropic population is beyond the mirror instability constraint. This result implies that some of the PCS solar wind is further heated, especially in the perpendicular direction to the background magnetic field if we combine the temperature observations in Figure 1(c). The possible heating mechanisms could be the prevalent magnetic reconnections around current sheet crossings (Lavraud et al. 2020; Phan et al. 2020, 2021), the turbulence in the inner heliosphere (Chen et al. 2021a), the switchbacks (Akhavan-Tafti et al. 2022), and/or other processes. Among these mechanisms, magnetic reconnection is the most likely heating
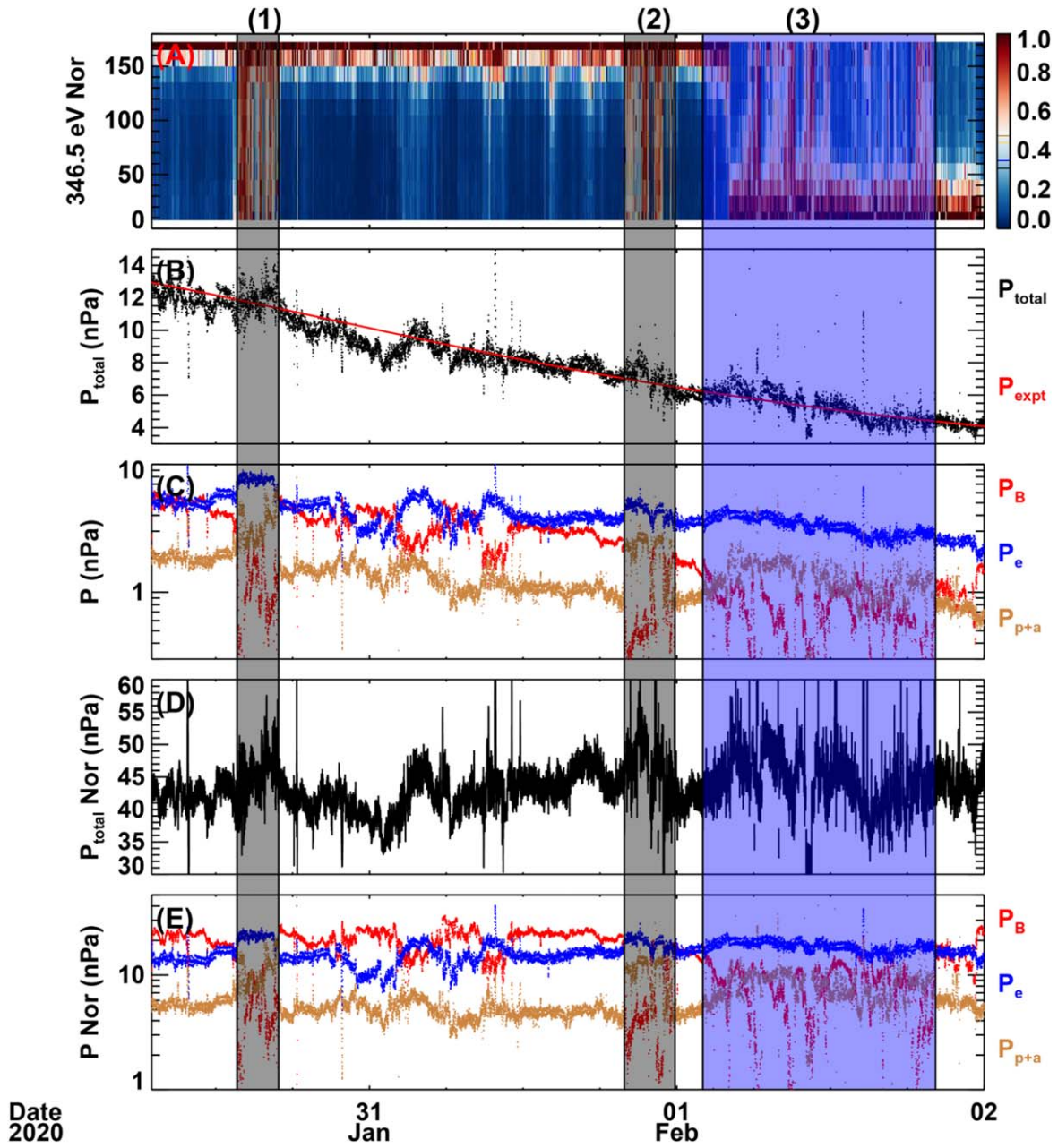
Figure 2. Pressure variations in the E4 streamer belt solar wind. From top to bottom, the panels show the normalized e-PAD at energy of 346.5 eV, total pressure (P_{total}) and expected total pressure (P_{expt}), pressure components (P_B, P_e, and P_{p+a}), normalized total pressure, and normalized pressure components. The three shaded regions and the blue dashed lines mark the high-β streamer belt solar wind and switchbacks, respectively, as in Figure 1.

mechanism due to its prevalence and efficiency to heat the plasma. As indicated by Chen et al. (2021a), the E4 streamer belt solar wind shows much lower Alfvénic turbulence energy flux, which may not be able to accelerate and heat the solar wind. In addition, the switchbacks are found in both the HPS and PCS solar wind, but the isotropic temperatures in the HPS solar wind imply that the switchbacks cannot heat the solar wind efficiently.

3.4. Helium Signatures

The helium signatures connect the in situ solar wind with its source regions at the Sun (e.g., Bochsler 2007; Aellig et al. 2001; Kasper et al. 2012; Huang et al. 2016b, 2018; Fu et al. 2018). In the fast solar wind, the helium abundance ratio

($A_{He} = N_\alpha / N_p \times 100\%$) usually increases, and the alpha–proton drift speed ($\Delta V_{\alpha p}$) is generally large and comparable to the local Alfvén speed (V_A), implying that the helium-rich population is from open magnetic field regions in the Sun (Borrini et al. 1981; Gosling et al. 1981; Marsch et al. 1982; Steinberg et al. 1996; Reisenfeld et al. 2001; Suess et al. 2009; Berger et al. 2011). However, in the slow solar wind, A_{He} varies with solar activity; i.e., the helium-poor population is usually observed at solar minimum, which could originate from the streamer belt, but the helium-rich population observed at solar maximum is primarily from active regions (Kasper et al. 2007, 2012; Alterman et al. 2018; Alterman & Kasper 2019). Additionally, $\Delta V_{\alpha p}$ is close to zero in the slow solar wind (Marsch et al. 1982; Steinberg et al. 1996; Reisenfeld et al. 2001; Berger et al. 2011). Further, studies
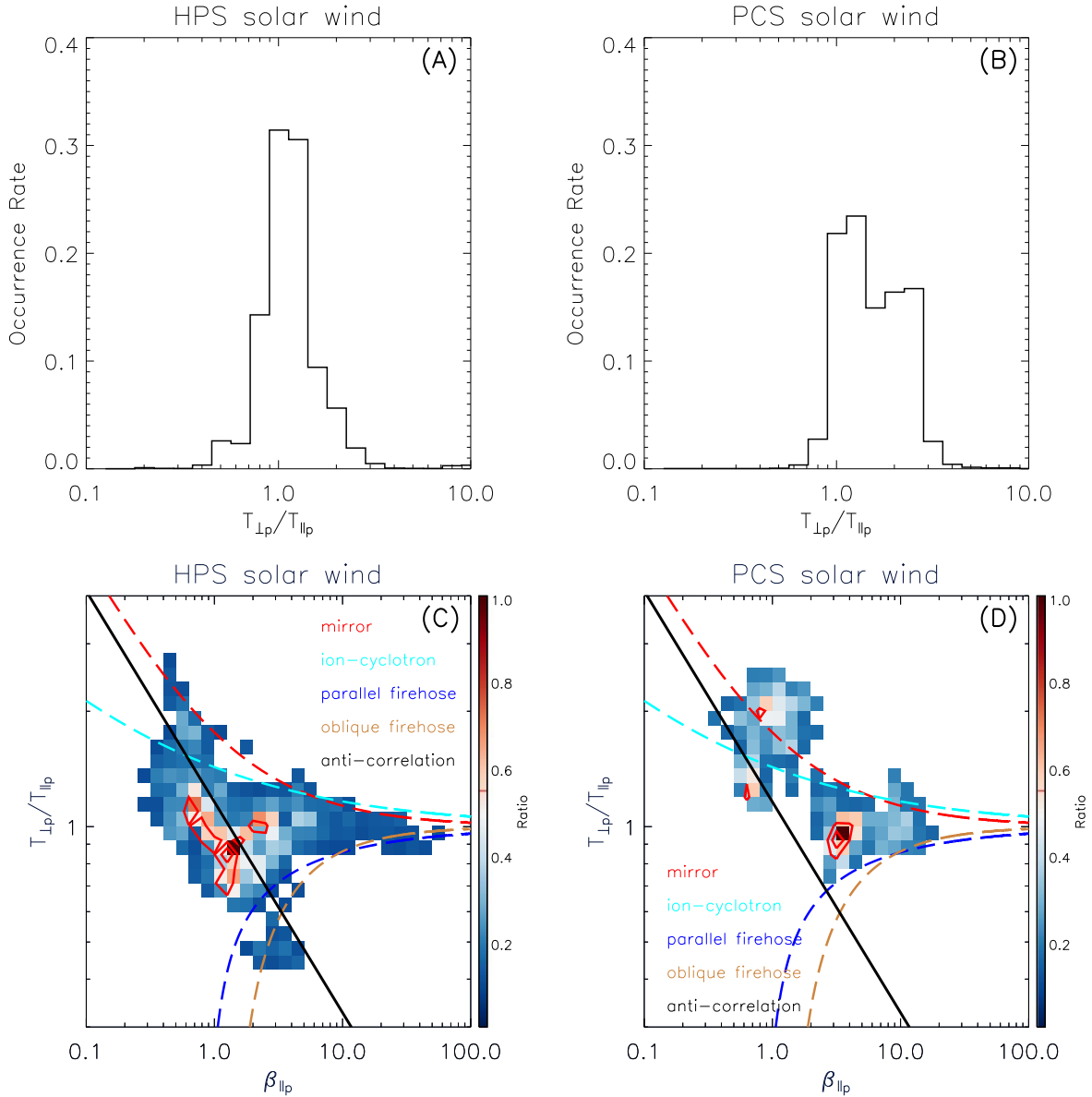
Figure 3. Temperature anisotropies in the E4 streamer belt solar wind. Panels (a) and (c) display the temperature anisotropy ($T_{\perp p}/T_{\parallel p}$) signatures in the HPS solar wind, and panels (b) and (d) show the same parameters in the PCS solar wind. Panels (a) and (b) present the occurrence rates of temperature anisotropies in the HPS and PCS solar winds, respectively. Panels (c) and (d) exhibit the temperature anisotropy versus parallel plasma β ($\beta_{\parallel p}$) in the HPS and PCS solar winds, respectively. The different colored dashed lines are instabilities, as indicated by the legend, and the black line is the anticorrelation relationship. The red contours indicate 50% and 75% measurements.

reveal approximate bimodal distributions of A_{He} versus $\Delta V_{\alpha p}/V_A$ in the solar wind observed around 1 au, with the high-A_{He} and high-$\Delta V_{\alpha p}/V_A$ population probably escaping directly along open magnetic field lines, as described by wave turbulence–driven models, whereas the low-A_{He} and low-$\Delta V_{\alpha p}/V_A$ population releases through magnetic reconnection processes (Ďurovcová et al. 2017, 2019; Fu et al. 2018, and references therein). Therefore, the helium signatures could help identify the possible origins of the HPS and PCS solar wind.

As described in Appendix A, we follow Reisenfeld et al. (2001) and Fu et al. (2018) to define the $\Delta V_{\alpha p}$ as the field-aligned differential speed, i.e., $\Delta V_{\alpha p} = (v_{\alpha r} - v_{pr})/\cos(\theta)$, where $v_{\alpha r}$ and v_{pr} are the radial speeds of the alpha particle and proton, respectively, and θ measures the angle of the magnetic field vector from the radial direction. Here we further require $\cos(\theta) = |B_r/B|$ to remove its dependency on the

magnetic field polarity, where B_r represents the radial magnetic field.

Figure 4 shows the distributions of A_{He} versus $\Delta V_{\alpha p}/V_A$ in the HPS (panel (a)) and PCS (panel (b)) solar wind during E4. The colors indicate the occurrence ratios, whereas the red contours represent 50% and 75% of measurements. In the HPS solar wind, we can see that the plasma is dominated by low $\Delta V_{\alpha p}/V_A$, but A_{He} varies from low to high values. The distribution is centered around $A_{He} = 1.5\%$ and $\Delta V_{\alpha p}/V_A = 0.35$, implying that the HPS solar wind mainly originates from a closed magnetic field region via magnetic reconnection processes. But the large A_{He} population indicates that some of the HPS solar wind comes from the open field region, which may be the leg/flank region of the helmet streamer (Suess et al. 2009). In contrast, the PCS solar wind is dominated by low A_{He} when the $\Delta V_{\alpha p}/V_A$ changes from small
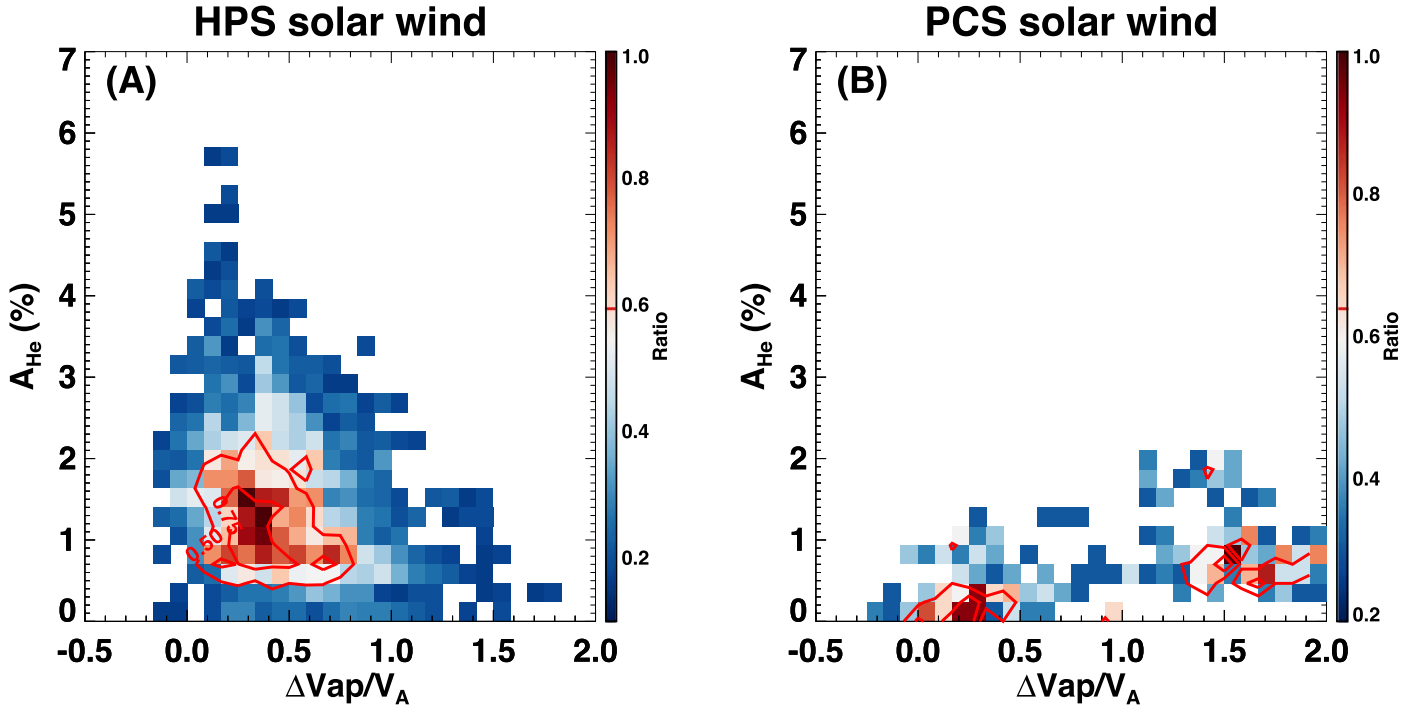
Figure 4. Distributions of helium abundance (A_{He}) vs. alpha–proton differential speed normalized by local Alfvén speed ($\Delta V_{\alpha p}/V_A$) in the E4 streamer belt solar wind. Panels (a) and (b) present the helium characteristics in the HPS and PCS solar wind, respectively. The colors indicate the occurrence ratios. The red contours in both panels represent 50% and 75% of measurements.

to large values. From panel (b), we can see that there are two populations in the PCS solar wind. One population has very low A_{He} ($\sim 0.2\%$) and small $\Delta V_{\alpha p}/V_A$ (~ 0.25), suggesting that the solar wind is from a closed magnetic field region via probably magnetic reconnection. The other population maintains low A_{He} ($\sim 0.7\%$) but large $\Delta V_{\alpha p}/V_A$ (~ 1.6), implying that the solar wind is also from a closed field region, but the alpha particles could be preferentially accelerated (Isenberg & Hollweg 1983; Kasper et al. 2017).

In addition, we note that the PCS solar wind shows two populations in Figures 3 and 4; thus, we would like to know if the two populations are intrinsically related to each other. In Figure 5, we plot the distribution of $\beta_{\parallel p}$ versus $\Delta V_{\alpha p}/V_A$ in the E4 PCS solar wind because the two parameters could significantly separate the two populations in their distributions. From this figure, we can see that $\Delta V_{\alpha p}/V_A$ is almost linearly associated with $\beta_{\parallel p}$. Therefore, the low-A_{He} and low-$\Delta V_{\alpha p}/V_A$ population in Figure 4 should have low $\beta_{\parallel p}$ but high $T_{\perp p}/T_{\parallel p}$ (i.e., the anisotropic population), whereas the low-A_{He} and high-$\Delta V_{\alpha p}/V_A$ population corresponds to the isotropic population in Figure 3. This is a really interesting result.

In the combination of all observations, we can infer that the non-pressure-balanced PCS solar wind has two populations. One population shows very low A_{He}, low $\Delta V_{\alpha p}/V_A$, and anisotropic $T_{\perp p}/T_{\parallel p}$ that is mirror-unstable. This part of the PCS solar wind should come from closed loops deep inside the streamer belt, probably via successive magnetic reconnection processes, which lead to the preferential heating of protons in perpendicular directions and then drive the mirror instability. In comparison, the other population has low but higher A_{He}, much higher $\Delta V_{\alpha p}/V_A$, and isotropic $T_{\perp p}/T_{\parallel p}$. This means that this population of the PCS solar wind could originate from closed regions of the streamer belt through magnetic reconnections, but the loops could be higher and fewer reconnection processes

may be needed to release the plasma, which may create some waves or turbulence that are favorable to further accelerate the alpha particles, but the exact reasons need a detailed investigation.

4. E4–E10 Results

In this section, we extend the above study to include E5–E10 observations. This is valuable to figure out whether the differences between the HPS and PCS solar wind are of significance.

Figure 6 gives an overview of the high-β streamer belt solar wind from E5 to E10. In each figure, the panels from top to bottom display the normalized e-PAD, β, total and expected pressure, normalized total pressure, Na/Np, $\Delta Vap/V_A$, and proton temperature anisotropy. The HPS and PCS solar wind are marked by blue and gray shaded regions, respectively. The details of the high-β streamer belt solar wind intervals are listed in Table 1 in Appendix C.

4.1. Pressure Variations

In this section, we will show that the non-pressure-balanced signature of the PCS solar wind is evidential.

In Figure 6, we mark several PCS solar wind intervals from E7 to E10 with black arrows. These intervals display profound pressure enhancements, which can be seen both from the comparison between P_{total} and P_{expt} in the third panel and from P_{total} Nor in the fourth panel in each figure. These distinct enhancements suggest that the PCS solar wind could be non-pressure-balanced structures.

Figure 7 presents more details on the pressure variations in the HPS and PCS solar wind. Panel (a) shows the distribution of β versus P_{total} Nor. Panel (b) exhibits the distribution of P_k Nor versus P_B Nor. In both panels, the colors indicate the
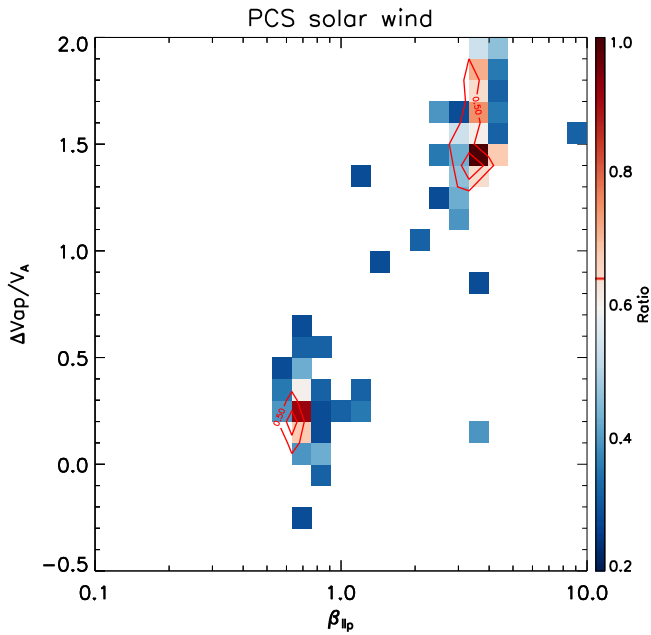
Figure 5. Distributions of parallel plasma β ($\beta_{\parallel p}$) vs. alpha–proton differential speed normalized by the local Alfvén speed ($\Delta V_{\alpha p}/V_A$) in the E4 PCS solar wind. The colors indicate the occurrence ratios. The red contours represent 50% and 75% of measurements.

occurrence ratios of the solar wind in E4–E10 below 0.25 au. The red and gold contours represent the HPS and PCS solar wind as listed in Table 1, respectively. In panel (b), the cyan dashed line represents P_B Nor + P_k Nor = 45 nPa, and the black dashed line suggests P_B Nor = P_k Nor.

From Figure 7(a), we can see that the HPS solar wind generally has large β from about one to several hundreds, but $P_{\rm total}$ Nor is around 45 nT with the distributions spread below $\beta \sim 10$. In the PCS solar wind, β is smaller, varying from 1 to about 60. The $P_{\rm total}$ Nor is around 45 nT above $\beta \sim 6$, but it is much larger than 45 nT below $\beta \sim 6$, which further supports the above statement that the PCS solar wind should be non-pressure-balanced structures. However, the origin of the pressure enhancements from $\beta \sim 1$ to 5 in the background solar wind is unknown, which may be the unidentified PCS solar wind because the criteria to select the PCS solar wind are generally strict in this work. In Figure 7(b), we can see that P_K Nor is larger than P_B Nor in both the HPS and PCS solar wind, as shown by the black dashed line, which is expected because the magnetic field strength usually depletes significantly around current sheet crossings. However, the total pressure enhancement in the PCS solar wind should be caused by the less reduced or unreduced magnetic pressure therein as compared with the HPS solar wind, as indicated by the cyan line.

As a conclusion, the HPS solar wind is roughly pressure-balanced, but the PCS solar wind shows an evidential non-pressure-balanced signature, and the enhancement of the total pressure in the PCS solar wind could be a result of the magnetic pressure not reducing significantly.

4.2. Temperature Anisotropy Characteristics

Figure 8 shows the temperature anisotropies in the streamer belt solar wind in E4–E10, with the same format as Figure 3. This figure displays similar temperature anisotropy characteristics as in Figure 3.

In the HPS solar wind, we can see that $T_{\perp p}/T_{\parallel p}$ is almost isotropic from panel (a), and the solar wind is well limited by the instabilities, with some exceeding the mirror limitation, as shown in panel (c). In comparison with the E4 result, we can see that the main distribution of $\beta_{\parallel p}$ is larger, implying that $T_{\parallel p}$ is higher in the following encounters when closer to the Sun, which is reasonable (Huang et al. 2020b). These results are consistent with the E4 result that the HPS solar wind is mostly in a thermal equilibrium state.

In the PCS solar wind, we can still see two populations in panel (d), but this signature is not noticeable in panel (b), which shows a broad distribution around $T_{\perp p}/T_{\parallel p} = 1$. Additionally, the plasma is also limited by the instabilities, but some of the anisotropic population is distributed beyond the mirror instability. This is also consistent with the E4 result that some PCS solar wind is experiencing preferential proton heating.

4.3. Helium Signatures

Figure 9 displays the helium signatures in the streamer belt solar wind in E4–E10, with the same format as Figure 4. It also shows similar results as E4, but the distributions are more complicated.

In the HPS solar wind, we can see that the major distribution is dominated by low-$A_{\rm He}$ ($\sim 1\%$) and low $\Delta V_{\alpha p}/V_A$ (around zero). But we can also see a low-$A_{\rm He}$ and high-$\Delta V_{\alpha p}/V_A$ ($|\Delta V_{\alpha p}/V_A| > 1$) population and high-$A_{\rm He}$ ($>4\%$) and low-$\Delta V_{\alpha p}/V_A$ population. This indicates that the HPS solar wind originates from both closed and open magnetic field regions at the Sun. The large positive $\Delta V_{\alpha p}/V_A$ implies that the alphas could be further accelerated (Isenberg & Hollweg 1983; Kasper et al. 2017), but the negative values infer that the alphas may be decelerated over distance during solar wind expansion (Neugebauer et al. 1994; Maneva et al. 2015; Mostafavi et al. 2022). The complicated variations of the helium signatures in the HPS solar wind suggest that the selected HPS solar wind intervals may contain plasma from extra source regions, and this also indicates the complex variations of the solar wind in the inner heliosphere.

In the PCS solar wind, the two populations are still distinctive, but the low-$A_{\rm He}$ and high-$\Delta V_{\alpha p}/V_A$ population shifts predominantly from positive $\Delta V_{\alpha p}/V_A$ values to negative ones. Therefore, the PCS solar wind should mainly come from the closed magnetic field regions of the streamer belt, but the alphas could experience either acceleration or deceleration processes during propagation, as stated above. In addition, we note that the linear relationship between $\Delta V_{\alpha p}/V_A$ and $\beta_{\parallel p}$ is roughly maintained (not shown) in the PCS solar wind, but temperature anisotropy populations are somewhat overlapped with each other, as shown in Figure 8. Thus, we display the temperature anisotropy distributions of the PCS solar wind with different $\Delta V_{\alpha p}/V_A$ in Figure 10. Panel (a) shows the PCS solar wind with low $\Delta V_{\alpha p}/V_A$ ($|\Delta V_{\alpha p}/V_A| < 0.8$), whereas panel (b) presents another population with high $\Delta V_{\alpha p}/V_A$ ($|\Delta V_{\alpha p}/V_A| > 0.8$). From this figure, we can see that the low-$\Delta V_{\alpha p}/V_A$ population has broader $T_{\perp p}/T_{\parallel p}$ distributions and a slightly more anisotropic population beyond mirror instability. One more interesting feature regarding the high-$\Delta V_{\alpha p}/V_A$ PCS solar wind is that the major temperature anisotropies seem to distribute along the anticorrelation line, as shown by the black line in panel (b), which mainly corresponds to the proton core behaviors. This implies that the low-$\Delta V_{\alpha p}/V_A$ PCS solar wind may be involved with proton
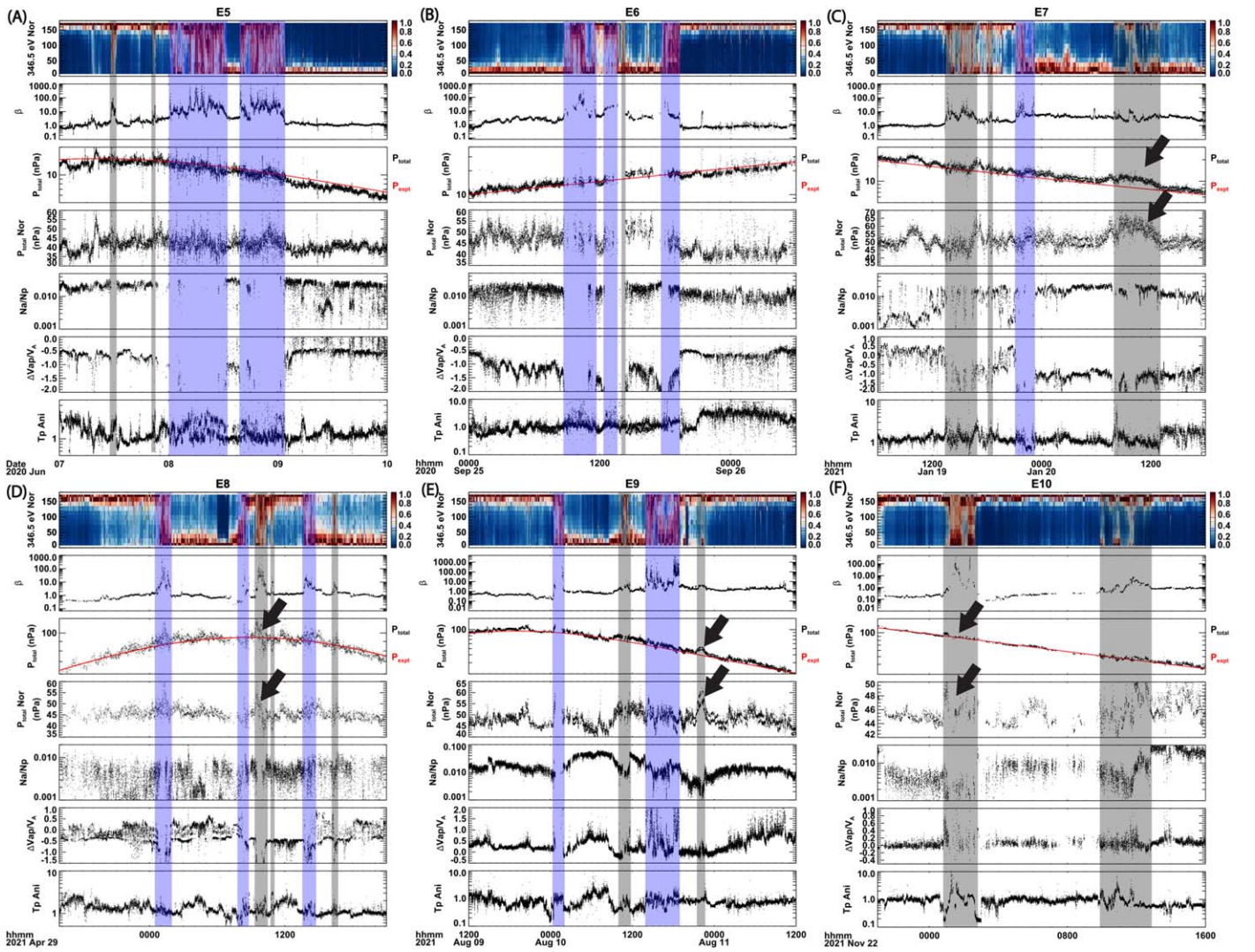
Figure 6. Overview of the high-β streamer belt solar wind from E5 to E10. In each figure, the panels from top to bottom show the normalized e-PAD at energy of 346.5 eV, plasma β, total and expected pressure, normalized total pressure, alpha-to-proton abundance ratio Na/Np, alpha–proton differential speed normalized by local Alfvén speed $\Delta Vap/V_A$, and proton temperature anisotropy. The blue shaded regions mark the HPS solar wind, whereas the gray shaded regions mark the PCS solar wind.

beam variations, and it is valuable to further investigate the differences of the velocity distribution functions in the two populations of the PCS solar wind.

As a result, the multi-event study in this section suggests that the PCS solar wind is different from the HPS solar wind. The features of the HPS solar wind are generally consistent with those observed at 1 au, but the temperature anisotropy and helium signatures are more complicated in the inner heliosphere. However, the PCS solar wind shows a non-pressure-balanced signature and has two populations that are involved with preferential proton heating and/or alpha acceleration/deceleration.

5. Discussion

Here we want to clarify that the PCS solar wind should not be magnetic holes. We note that Chen et al. (2021b) used similar criteria, including reduced magnetic field, enhanced density, high plasma β, and PCS crossing, to identify this kind of solar wind as macro magnetic holes, which could be caused by the HCS ripples. The magnetic holes have been studied for

several decades since they were first reported by Turner et al. (1977). In general, the magnetic coronal holes are isolated, pressure-balanced structures with the magnetic field strength significantly reduced, and they are more often observed in a fast solar wind or an environment with high β and $T_{\perp p}/T_{\parallel p}$ (e.g., Stevens & Kasper 2007; Chen et al. 2021b, and references therein).

However, our result suggests that the PCS solar wind should be non-pressure-balanced structures, which is in contrast to the most distinguishing characteristic of magnetic holes. Moreover, in the PCS solar wind, the kinetic pressure is larger and the magnetic pressure is smaller than in the ambient solar wind. But the total pressure enhancement in the PCS solar wind is mainly caused by the less decreased magnetic pressure as compared with the HPS solar wind, as shown in Figure 7(b); this further indicates that the magnetic field in the PCS solar wind does not reduce very significantly, which is also in contrast to the primary definition of magnetic holes. In addition, as discussed by Phan et al. (2021), the PCS crossings are likely generated by the traveling large plasma blobs bulging
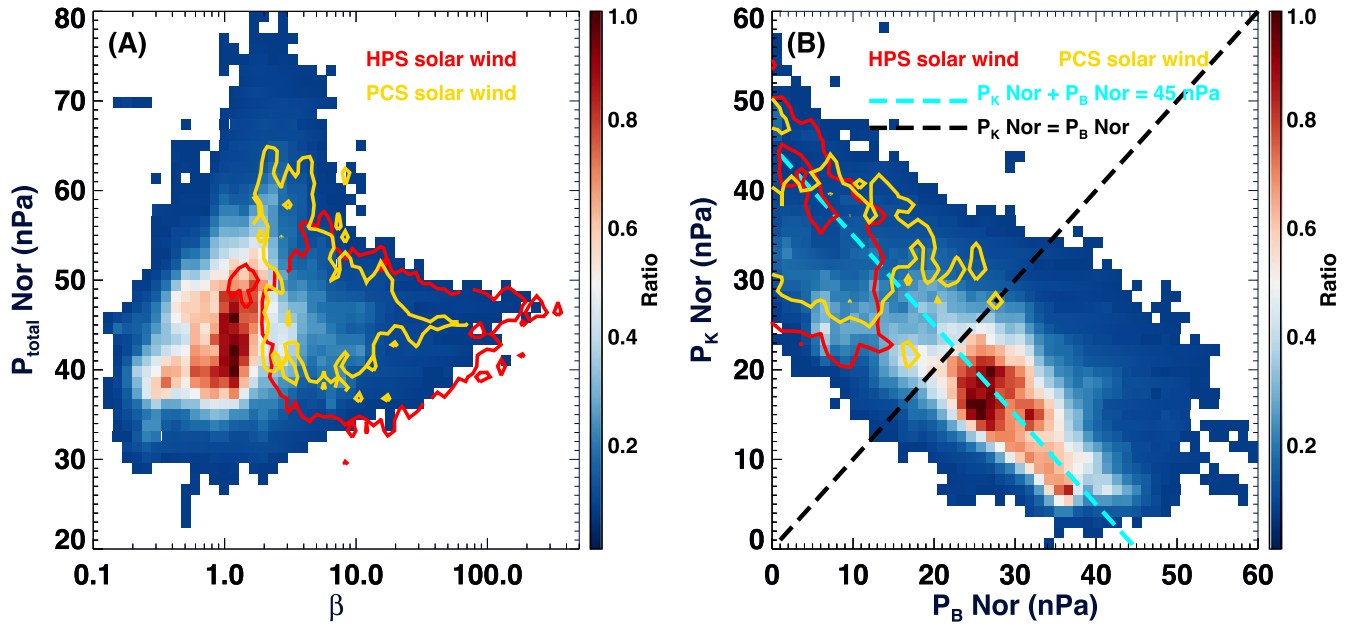
Figure 7. Pressure variations in E4–E10. Panel (a) shows the distribution of normalized total pressure (P_{total} Nor) vs. plasma β. Panel (b) shows the distribution of normalized thermal pressure (P_k Nor) vs. normalized magnetic pressure (P_B Nor). In both panels, the colors mean the occurrence ratios of the solar wind. The red and gold contours indicate the HPS and PCS solar winds, respectively. In panel (b), the cyan dashed line represents P_B Nor + P_k Nor = 45 nPa, and the black dashed line suggests P_B Nor = P_k Nor.

Table 1
The High-β Streamer Belt Solar Wind Intervals in Each Encounter

Encounter	No.	Start Time (UT)	End Time (UT)	Current Sheet Crossing
E4	01	2020-01-30/13:40:00	2020-01-30/16:54:20	PCS
	02	2020-01-31/19:56:00	2020-01-31/23:52:00	PCS
	03	2020-02-01/02:44:00	2020-02-01/20:12:00	HCS
E5	04	2020-06-07/11:21:00	2020-06-07/12:24:00	PCS
	05	2020-06-07/20:25:00	2020-06-07/21:09:00	PCS
	06	2020-06-08/00:12:00	2020-06-08/12:40:00	HCS
	07	2020-06-08/15:42:00	2020-06-09/01:32:00	HCS
E6	08	2020-09-25/08:42:00	2020-09-25/11:42:00	HCS
	09	2020-09-25/12:26:20	2020-09-25/13:49:10	HCS
	10	2020-09-25/13:52:20	2020-09-25/14:41:30	PCS
	11	2020-09-25/17:40:30	2020-09-25/18:28:40	HCS
E7	12	2021-01-19/13:31:00	2021-01-19/16:46:00	PCS
	13	2021-01-19/18:16:00	2021-01-19/18:31:00	PCS
	14	2021-01-19/21:08:30	2021-01-19/23:26:00	HCS
	15	2021-01-20/07:55:30	2021-01-20/13:32:00	PCS
E8	16	2021-04-29/00:44:50	2021-04-29/01:51:10	HCS
	17	2021-04-29/08:14:40	2021-04-29/08:51:30	HCS
	18	2021-04-29/09:24:40	2021-04-29/10:22:40	PCS
	19	2021-04-29/10:48:10	2021-04-29/10:57:30	PCS
	20	2021-04-29/13:40:10	2021-04-29/14:23:40	HCS
	21	2021-04-29/16:15:40	2021-04-29/16:38:20	PCS
E9	22	2021-08-10/00:30:00	2021-08-10/01:54:00	HCS
	23	2021-08-10/10:34:00	2021-08-10/11:38:00	PCS
	24	2021-08-10/13:52:00	2021-08-10/19:50:00	HCS
	25	2021-08-10/21:43:00	2021-08-10/22:56:00	PCS
E10	26	2021-11-22/01:10:00	2021-11-22/02:37:00	PCS
	27	2021-11-22/09:58:00	2021-11-22/12:10:40	PCS
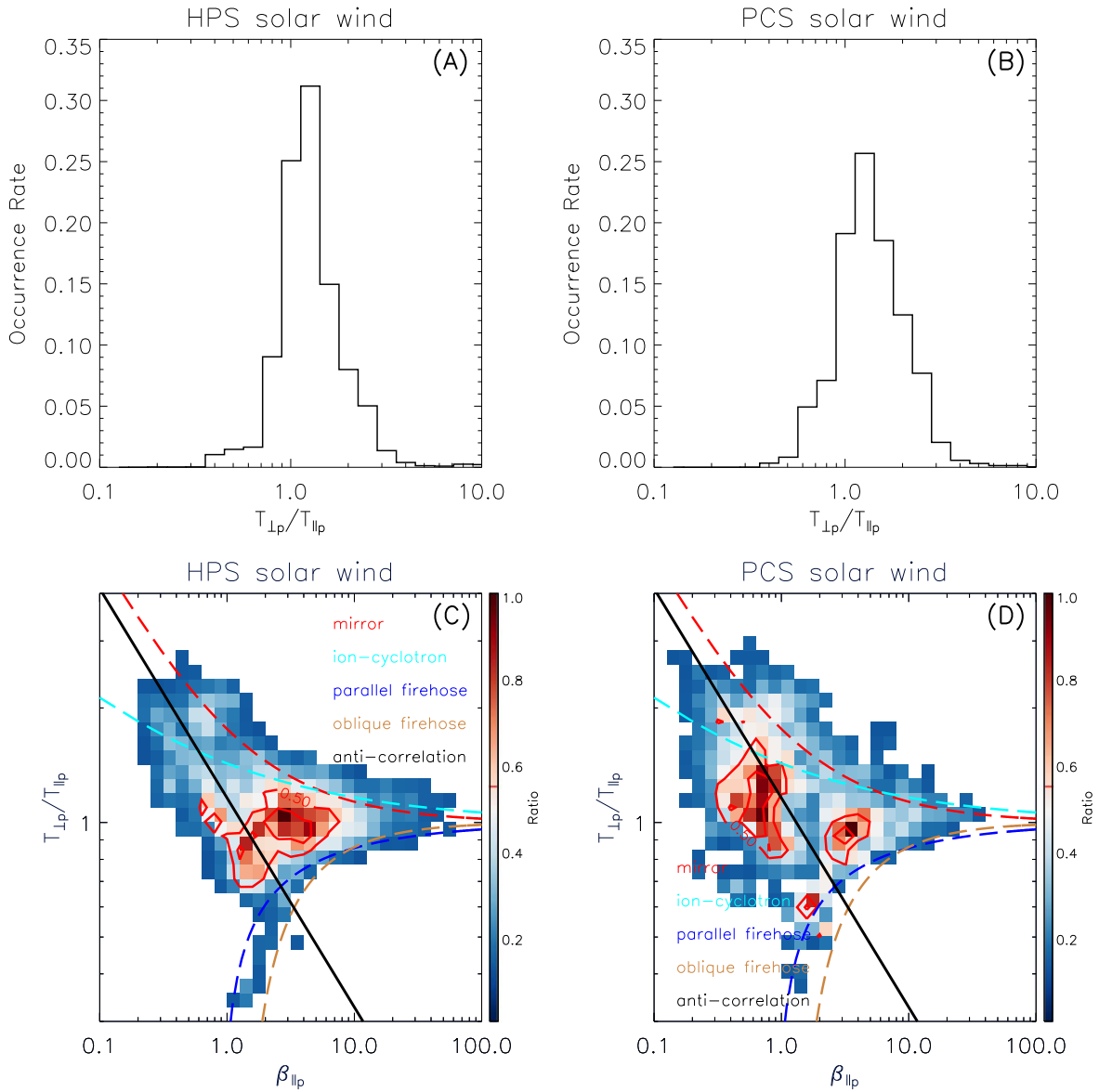
Figure 8. Temperature anisotropies in the streamer belt solar wind from E4 to E10. This figure has the same format as Figure 3.

onto both sides of the HCS crossings based on their signatures of long duration and recurrent appearance. Thus, the PCS crossings may not be associated with a rippled HCS. As a result, we suggest that the PCS solar wind should not be identified as magnetic holes, especially when its source is clear; this is important to correctly understand the solar wind properties. Additionally, the investigations of kinetic- and small-scale magnetic holes (e.g., Huang et al. 2021; Yu et al. 2021, 2022; Zhou et al. 2022) may need to verify whether they are associated with the PCS solar wind.

Moreover, we discuss some of the slow solar wind observations by PSP that are associated with this work. We note that the 4 yr of discoveries at solar cycle minimum by PSP have been thoroughly reviewed by Raouafi et al. (2023). As the PSP approaches the solar atmosphere, new features of the slow solar wind have been uncovered near the Sun. First, PSP has detected several sub-Alfvénic solar wind intervals since it entered the Alfvén critical surface in E8 (Bandyopadhyay et al. 2021; Kasper et al. 2021; Zank et al. 2022; Zhao et al. 2022). However, the selected streamer belt solar wind intervals have

no overlap with the sub-Alfvénic solar wind intervals due to the streamer belt solar wind being characterized by high plasma β, whereas the sub-Alfvénic solar wind is characterized by low plasma β. Further, based on our preliminary analysis of four long intervals of sub-Alfvénic solar wind,[13] we suggest that the sub-Alfvénic solar wind could be pressure-balanced structures, implying that they are well-evolved solar wind streams that probably originate from pseudostreamers in the Sun (Kasper et al. 2021). Second, PSP observed a prevalent Alfvénic slow solar wind in the past 4 yr. The Alfvénic slow solar wind is a slow wind with high Alfvénicity, which is a typical feature of the fast solar wind rather than the slow one. The Alfvénic slow solar wind is not commonly observed at 1 au, and studies suggest that it should come from the coronal holes in the Sun (D'Amicis & Bruno 2015; D'Amicis et al. 2018; Wang et al. 2019). The PSP observations indicate a pervasive Alfvénic

---

[13] Interval 1 (E8): 2021 April 28 09:33–2021 April 28 14:42 UT; interval 2 (E9): 2021 August 09 21:30–2021 August 10 00:24 UT; interval 3 (E10): 2021 November 21 21:23–2021 November 22 00:57 UT; interval 4 (E10): 2021 November 22 02:40–2021 November 22 09:52 UT.
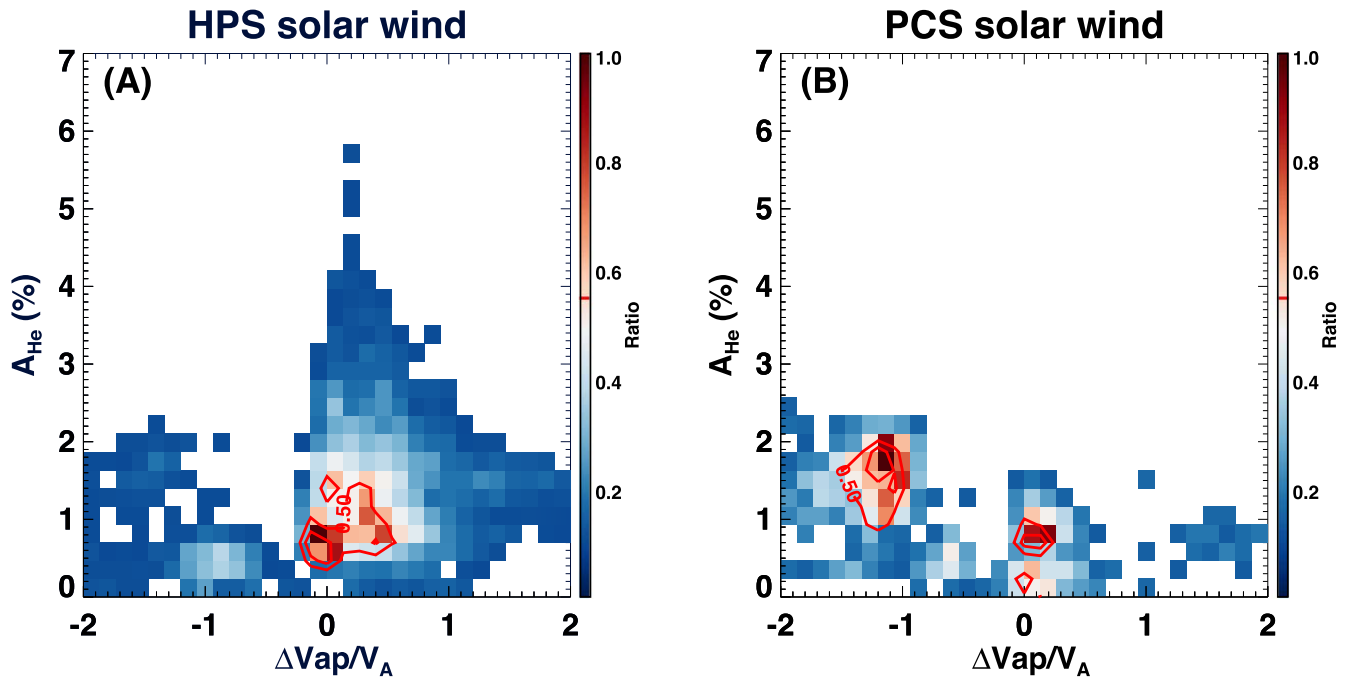
Figure 9. Distributions of helium abundance (A_{He}) vs. alpha–proton differential speed normalized by local Alfvén speed ($\Delta V_{\alpha p}/V_A$) in the streamer belt solar wind from E4 to E10. This figure has the same format as Figure 4.
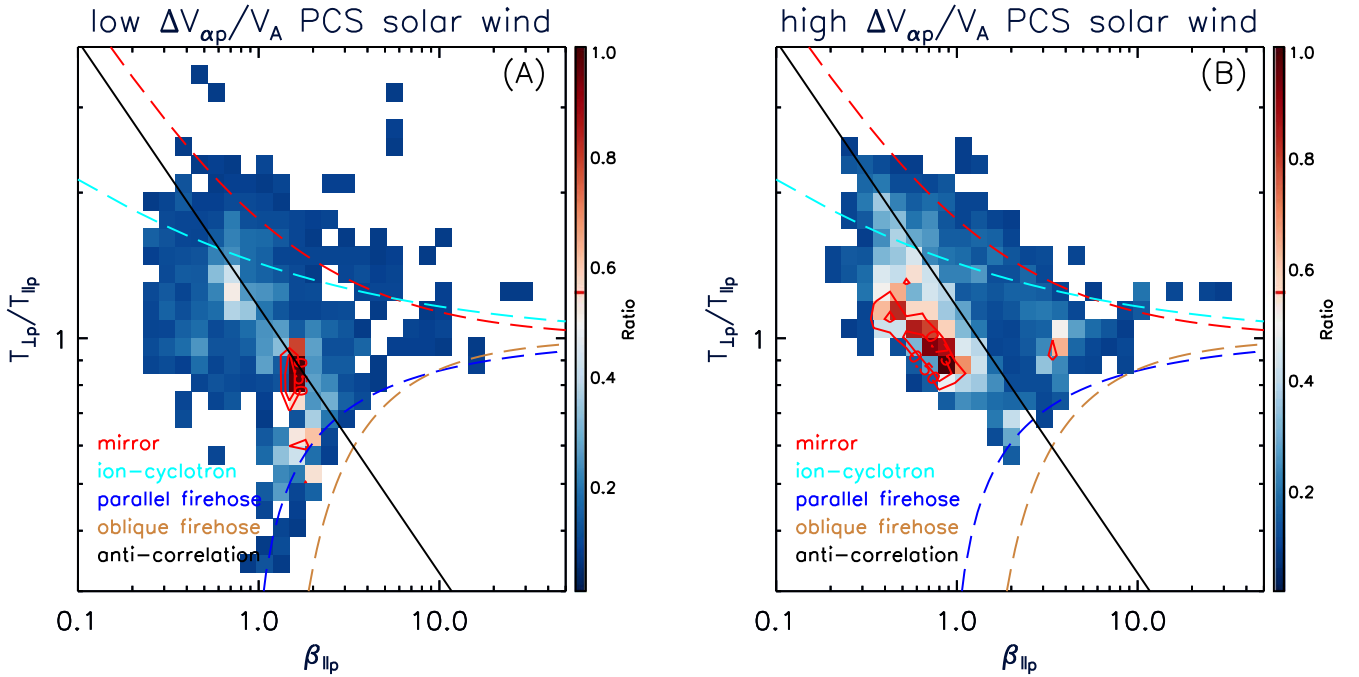
Figure 10. Temperature anisotropy distributions of the PCS solar wind with different $\Delta V_{\alpha p}/V_A$ from E4 to E10. This figure has a similar format as the bottom panels of Figure 3.

slow solar wind in the inner heliosphere, and case studies confirm its origins from coronal holes (Bale et al. 2019; Griton et al. 2021). However, Huang et al. (2020a) showed that the highly Alfvénic slow solar wind shares similar temperature anisotropy and helium abundance properties with the regular slow solar wind and thus may have multiple origins based on statistical analysis. In addition, the current sub-Alfvénic solar wind observed by PSP is also the Alfvénic slow solar wind (Zank et al. 2022; Zhao et al. 2022). The streamer belt solar wind generally has low Alfvénicity (Huang et al. 2020a; Zhao

et al. 2022), and it would be valuable to further disclose the differences of slow solar wind with different Alfvénicities. Third, the slow solar wind is very dynamic in the near-Sun environment, as introduced in Section 1. The spatial and temporal variabilities of the slow solar wind are further increased due to multiple current sheet crossings (Lavraud et al. 2020; Szabo et al. 2020), magnetic reconnection exhausts (Phan et al. 2021), small flux ropes (Chen et al. 2021c; Zhao et al. 2021; Réville et al. 2022; Chen et al. 2023), turbulences (Chen et al. 2021a; Zank et al. 2022; Zhao et al. 2022),

switchbacks (Kasper et al. 2019; Dudok de Wit et al. 2020; Fisk & Kasper 2020; Horbury et al. 2020; Zank et al. 2020), and so on. As a result, investigating the slow solar wind that either originates from the same source region or shares similar properties could reduce the uncertainty in such studies, and the pressure, temperature anisotropy, and alpha characteristics could be crucial to understanding the underlying mechanisms of the slow solar wind.

6. Summary

In this work, using the PSP observations from E4 to E10, we identify the streamer belt solar wind from enhancements in plasma β, and we further use electron pitch angle distributions to separate it into the HPS solar wind around full HCS crossings and the PCS solar wind in the vicinity of PCS crossings. Focusing on E4 observations, we find that the two kinds of solar wind show different characteristics of pressure, temperature anisotropy, and helium distribution. By extending this study to E10, we figure out more complicated variations of the above parameters. The major results are summarized as follows.

1. The HPS solar wind is generally pressure-balanced, but the PCS solar wind should be non-pressured-balanced structures. The total pressure of the PCS solar wind evidently increases, which is caused by the fact that the magnetic pressure therein does not significantly reduce as compared with the HPS solar wind.

2. The HPS solar wind is mostly in a thermal equilibrium state, but the PCS solar wind has two populations. One population of the PCS solar wind has isotropic proton temperatures, but the other population shows anisotropic signatures with some solar wind being mirror-unstable.

3. The HPS solar wind is characterized by low $\Delta V_{\alpha p}/V_A$, whereas the PCS solar wind is dominated by low A_{He}. The HPS solar wind shows low $\Delta V_{\alpha p}/V_A$, but its A_{He} covers low-to-high values. However, the PCS solar wind has two populations, with one population distinguished by low A_{He} and low $\Delta V_{\alpha p}/V_A$ and the other population displaying low A_{He} but high $\Delta V_{\alpha p}/V_A$. Further, the low-A_{He} and low-$\Delta V_{\alpha p}/V_A$ population relates to anisotropic temperatures, but the low-A_{He} and high-$\Delta V_{\alpha p}/V_A$ population is almost isotropic. Furthermore, the multi-event study reveals more complicated variations in the inner heliosphere.

Combining all of the observations, we can conclude that the HPS solar wind is similar to that observed at 1 au and beyond, which is a pressure-balanced structure with a thermal equilibrium state and regular helium signature, implying that the HPS solar wind comes from both closed and open magnetic field regions of the streamer belt and is generally well evolved. However, the PCS solar wind is a non-pressure-balanced structure that has two populations. One population exhibits very low A_{He}, low $\Delta V_{\alpha p}/V_A$, and anisotropic $T_{\perp\,p}/T_{\parallel p}$ that is mirror-unstable, implying that it originates from closed loops deep inside the streamer belt, probably via successive magnetic reconnection processes, which preferentially heat protons in perpendicular directions and then possibly drive the mirror instability. In comparison, the other population has low but higher A_{He}, much higher $\Delta V_{\alpha p}/V_A$, and isotropic $T_{\perp\,p}/T_{\parallel p}$, suggesting that this population is from closed regions of the streamer belt through magnetic reconnections, but the loops

locate at higher altitude, and fewer reconnections are needed to release the plasma. Consequently, we draw another conclusion that the PCS solar wind should not be magnetic holes.

Appendix A
Parameters

The electron pressure $P_e = n_e\,k_B\,T_e$, proton and alpha pressure $P_{p+\alpha} = n_p\,k_B\,T_p + n_\alpha\,k_B\,T_\alpha$, total kinetic pressure $P_k = P_e + P_{p+\alpha}$, magnetic pressure $P_B = B^2/2\mu_0$, and total pressure $P_{total} = P_k + P_B$. In the equations, μ_0 is the vacuum magnetic permeability, k_B is the Boltzmann constant, B is the magnetic field strength, and n_i and T_i are the number density and temperature of the particle i species, where i is e, p, and α for electron, proton, and alpha particles, respectively.

The subscripts $\perp$ and $\parallel$ represent the perpendicular and parallel directions with respect to the ambient magnetic field B. Here $T_{\perp p}$, $T_{\parallel p}$, and $T_{\perp p}/T_{\parallel p}$ are the perpendicular proton temperature, parallel proton temperature, and proton temperature anisotropy, respectively. Here $\beta_{\parallel p} = 2\mu_0\,n_p\,k_B\,T_{\parallel p}/B^2$ is the parallel proton β, where $\beta = 2\mu_0\,n_p\,k_B\,T_p/B^2$ is the plasma β.

In addition, B_r and R_S are the radial component of the magnetic field and heliocentric distance, respectively; N_α/N_p is the alpha-to-proton number density ratio; and $A_{He} = N_\alpha/N_p \times 100\%$ measures the helium abundance ratio. Moreover, the alpha–proton differential speed is $\Delta V_{\alpha p} = (v_{\alpha r} - v_{pr})/\cos(\theta)$, where $v_{\alpha\,r}$ and v_{pr} are the radial speeds of the alpha particle and proton, respectively, and $\cos(\theta) = |B_r/B|$ is used to ensure that the derived differential speed is independent with magnetic field polarity (Reisenfeld et al. 2001; Fu et al. 2018). Besides, the local Alfvén speed is calculated with $V_A = |B|/\sqrt{\mu_0(N_p m_p + N_\alpha m_\alpha)}$, where m_p and m_α are the mass of the proton and alpha particles, respectively. In the calculations, we use the electron density derived from the analysis of the plasma QTN spectrum measured by the FIELDS Radio Frequency Spectrometer (Pulupa et al. 2017; Moncuquet et al. 2020) to replace N_p by assuming that A_{He} is 4%, which does not significantly change the V_A, as A_{He} generally varies from 1% to 8% (Liu et al. 2021; Mostafavi et al. 2022).

Appendix B
Radial Evolution of Pressures

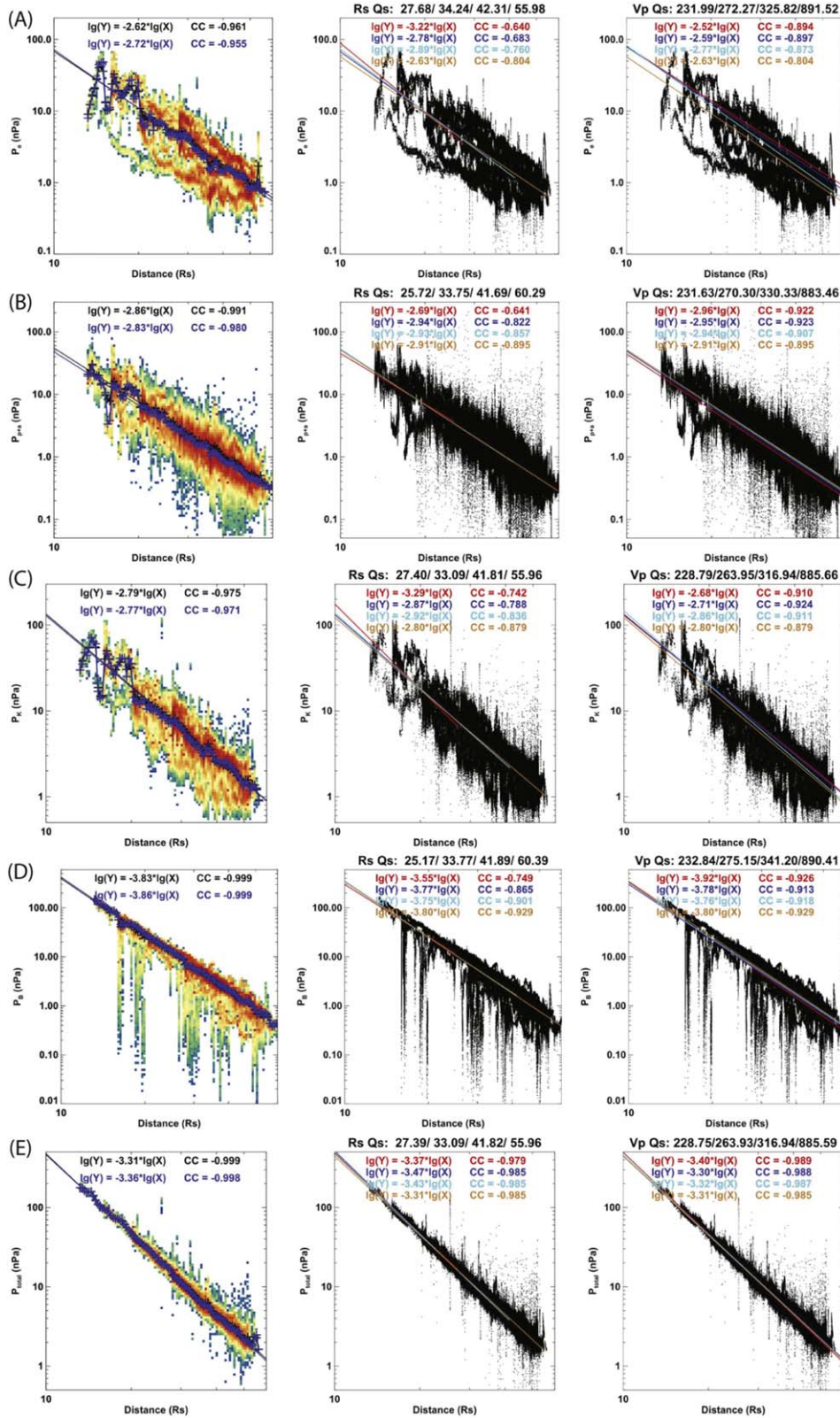Figure 11 shows the radial evolution of the pressure components of all solar wind from E4 to E12 below 0.25 au. From top to bottom, rows (a)–(e) present the radial evolution of electron pressure P_e, proton and alpha pressure $P_{p+\alpha}$, total kinetic pressure P_k, magnetic pressure P_B, and total pressure P_{total}. In each row, the left panel shows the pressure component, with the

Figure 11. Radial evolution of the pressure components of all solar wind from E4 to E12 below 0.25 au. From top to bottom, rows (a)–(e) present the radial evolution of electron pressure P_e, proton and alpha pressure $P_{p+\alpha}$, total kinetic pressure P_k, magnetic pressure P_B, and total pressure P_{total}. In each row, the left panel shows the pressure component, with the color indicating the occurrence ratio of the data points. The black and blue lines represent the fitted results based on the mean and median values of the pressure component at each distance bin, respectively. The fitted evolution indices and correlated coefficients are presented accordingly. The middle and right panels show the fittings based on the four distance quantiles and four speed quantiles, respectively. In both panels, the red, blue, cyan, and brown lines indicate the fitting results according to the first (25%), second (50%), third (75%), and fourth (100%) quantiles, with the fitted evolution indices and correlated coefficients presented accordingly.

color indicating the occurrence ratio of the data points. The black and blue lines represent the fitted results based on the mean and median values of the pressure component at each distance bin, respectively. The fitted evolution indices and correlated coefficients are presented accordingly. The middle and right panels show the fittings based on the four distance quantiles (as shown at the top with units of R_S) and four speed quantiles (as shown at the top with units of km s^{-1}), respectively. In both panels, the red, blue, cyan, and brown lines indicate the fitting results according to the first (25%), second (50%), third (75%), and fourth (100%) quantiles, with the fitted evolution indices and correlated coefficients presented accordingly. We use a power-law function to fit the radial evolution of each pressure component.

From this figure, we can see that the radial evolution of the pressure components varies with both heliocentric distance and solar wind speed, but the fitting results are comparable, and the correlation coefficients are pretty high. In this work, we do not focus on the variations with different distance and speed ranges; thus, we select the fitting results with higher correlation coefficients in the left panel in each row for normalization. Consequently, we choose the power-law indices of P_e, $P_{p+\alpha}$, P_k, P_B, and P_{total} to be -2.62, -2.86, -2.79, -3.83, and -3.31, respectively.

Moreover, the ideal spherical adiabatic expansion predicts that the magnetic field strength B and ion density n decrease as R^{-2} for a solar wind expanding with constant speed. Further, with an ideal polytropic index $\gamma = 5/3$, the kinetic pressure and total temperature follow the relationship of $P_k \propto n^\gamma \propto R^{-10/3}$ and $T \propto n^{\gamma-1} \propto R^{-4/3}$, respectively, whereas the ion pressures approximately follow $P_i \propto R^{-10/3}$ as P_k, and the magnetic pressure follows $P_B \propto B^2 \propto R^{-4}$. For the total pressure $P_{total} = P_k + P_B$, we can derive that its radial power-law index should vary between that for P_B and P_k, i.e., -4 to $-10/3$. As the solar wind in interplanetary space generally has plasma $\beta > 1$, the radial power-law index of P_{total} is expected to be close to $-10/3$.

In comparison with our fitting results, we can see that $P_{total} \propto R^{-3.31}$ and $P_B \propto R^{-3.83}$ are very close to the prediction of adiabatic expansions, but the ion pressure components and total kinetic pressure show flatter slopes. This indicates that the solar wind observed by PSP is generally experiencing adiabatic expansion in the inner heliosphere; however, the ion pressures do not match well with the adiabatic expansion predictions, which is possibly caused by the stronger anisotropic heating of ions in the near-Sun environment (Huang et al. 2020b).

Appendix C
The Streamer Belt Solar Wind Intervals

Table 1 lists all of the high-β streamer belt solar wind intervals from E4 to E10 as shown in Figures 1 and 6. From left to right, the columns indicate the PSP encounter, the number of the selected interval, the start time, the end time, and the type of current sheet crossing. As a summary, there are 12 HCS crossings and 15 PCS crossings.

ORCID iDs

Jia Huang ⓘ https://orcid.org/0000-0002-9954-4707
J. C. Kasper ⓘ https://orcid.org/0000-0002-7077-930X
Davin E. Larson ⓘ https://orcid.org/0000-0001-5030-6030
Michael D. McManus ⓘ https://orcid.org/0000-0001-6077-4145
P. Whittlesey ⓘ https://orcid.org/0000-0002-7287-5098
Roberto Livi ⓘ https://orcid.org/0000-0002-0396-0547
Ali Rahmati ⓘ https://orcid.org/0000-0003-0519-6498
Orlando Romeo ⓘ https://orcid.org/0000-0002-4559-2199
K. G. Klein ⓘ https://orcid.org/0000-0001-6038-1923
Weijie Sun ⓘ https://orcid.org/0000-0001-5260-658X
Bart van der Holst ⓘ https://orcid.org/0000-0001-5260-3944
Zhenguang Huang ⓘ https://orcid.org/0000-0003-1674-0647
Lan K. Jian ⓘ https://orcid.org/0000-0002-6849-5527
Adam Szabo ⓘ https://orcid.org/0000-0003-3255-9071
J. L. Verniero ⓘ https://orcid.org/0000-0003-1138-652X
C. H. K. Chen ⓘ https://orcid.org/0000-0003-4529-3620
B. Lavraud ⓘ https://orcid.org/0000-0001-6807-8494
Mingzhe Liu ⓘ https://orcid.org/0000-0003-2981-0544
Samuel T. Badman ⓘ https://orcid.org/0000-0002-6145-436X
Tatiana Niembro ⓘ https://orcid.org/0000-0001-6692-9187
Kristoff Paulson ⓘ https://orcid.org/0000-0002-5699-090X
M. Stevens ⓘ https://orcid.org/0000-0002-7728-0085
A. W. Case ⓘ https://orcid.org/0000-0002-3520-4041
Marc Pulupa ⓘ https://orcid.org/0000-0002-1573-7457
Stuart D. Bale ⓘ https://orcid.org/0000-0002-1989-3596
J. S. Halekas ⓘ https://orcid.org/0000-0001-5258-6128

References

Aellig, M. R., Lazarus, A. J., & Steinberg, J. T. 2001, GeoRL, 28, 2767
Akhavan-Tafti, M., Kasper, J., Huang, J., & Thomas, L. 2022, ApJL, 937, L39
Alterman, B. L., & Kasper, J. C. 2019, ApJL, 879, L6
Alterman, B. L., Kasper, J. C., Stevens, M. L., & Koval, A. 2018, ApJ, 864, 112
Badman, S. T., Bale, S. D., Martinez Oliveros, J. C., et al. 2020, ApJS, 246, 23
Bale, S. D., Badman, S. T., Bonnell, J. W., et al. 2019, Natur, 576, 237
Bale, S. D., Goetz, K., Harvey, P. R., et al. 2016, SSRv, 204, 49
Bale, S. D., Horbury, T. S., Velli, M., et al. 2021, ApJ, 923, 174
Bandyopadhyay, R., Matthaeus, W. H., McComas, D. J., et al. 2021, A&A, 650, L4
Belcher, J. W., & Davis, L., Jr. 1971, JGR, 76, 3534
Belcher, J. W., Davis, L., Jr., & Smith, E. J. 1969, JGR, 74, 2302
Berger, L., Wimmer-Schweingruber, R. F., & Gloeckler, G. 2011, PhRvL, 106, 151103
Bochsler, P. 2007, A&ARv, 14, 1
Borrini, G., Gosling, J. T., Bame, S. J., Feldman, W. C., & Wilcox, J. M. 1981, JGR, 86, 4565
Burlaga, L. F. 1971, SSRv, 12, 600
Burlaga, L. F., Scudder, J. D., Klein, L. W., & Isenberg, P. A. 1990, JGR, 95, 2229
Case, A. W., Kasper, J. C., Stevens, M. L., et al. 2020, ApJS, 246, 43
Chen, C., Chandran, B., Woodham, L., et al. 2021a, A&A, 650, L3
Chen, C., Liu, Y. D., & Hu, H. 2021b, ApJ, 921, 15
Chen, Y., Hu, Q., Allen, R. C., & Jian, L. K. 2023, ApJ, 943, 33
Chen, Y., Hu, Q., Zhao, L., Kasper, J. C., & Huang, J. 2021c, ApJ, 914, 108
Cranmer, S. R., & Cranmer, S. R. 2019, Oxford Research Encyclopedia of Physics (Oxford: Oxford Univ. Press),
Crooker, N. U., Huang, C.-L., Lamassa, S. M., et al. 2004, JGRA, 109, A03107
D'Amicis, R., & Bruno, R. 2015, ApJ, 805, 84
D'Amicis, R., Matteini, L., & Bruno, R. 2018, MNRAS, 483, 4665
Dudok de Wit, T., Krasnoselskikh, V. V., Bale, S. D., et al. 2020, ApJS, 246, 39
Ďurovcová, T., Němeček, Z., & Šafránková, J. 2019, ApJ, 873, 24
Ďurovcová, T., Šafránková, J., Němeček, Z., & Richardson, J. 2017, ApJ, 850, 164
Finley, A. J., McManus, M. D., Matt, S. P., et al. 2020, A&A, 650, A17
Fisk, L. A., & Kasper, J. C. 2020, ApJL, 894, L4
Foullon, C., Lavraud, B., Luhmann, J. G., et al. 2011, ApJ, 737, 16
Fox, N. J., Velli, M. C., Bale, S. D., et al. 2016, SSRv, 204, 7
Fu, H., Madjarska, M. S., Li, B., Xia, L., & Huang, Z. 2018, MNRAS, 478, 1884
Gary, S. P. 1993, Theory of Space Plasma Microinstabilities (Cambridge: Cambridge Univ. Press)
Gosling, J. T., Borrini, G., Asbridge, J. R., et al. 1981, JGR, 86, 5438
Griton, L., Rouillard, A. P., Poirier, N., et al. 2021, ApJ, 910, 63
Halekas, J. S., Whittlesey, P. L., Larson, D. E., et al. 2021, A&A, 650, A15
He, J., Tu, C., Marsch, E., Bourouaine, S., & Pei, Z. 2013, ApJ, 773, 72

Hellinger, P., Trávníček, P., Kasper, J. C., & Lazarus, A. J. 2006, GeoRL, 33, L09101
Horbury, T. S., Woolley, T., Laker, R., et al. 2020, ApJS, 246, 45
Huang, J., Kasper, J. C., Fisk, L. A., et al. 2023, arXiv:2301.10374
Huang, J., Kasper, J. C., Stevens, M., et al. 2020a, arXiv:2005.12372
Huang, J., Kasper, J. C., Vech, D., et al. 2020b, ApJS, 246, 70
Huang, J., Liu, Y. C.-M., Klecker, B., & Chen, Y. 2016a, JGRA, 121, 19
Huang, J., Liu, Y. C.-M., Peng, J., et al. 2018, JGRA, 123, 7167
Huang, J., Liu, Y. C.-M., Qi, Z., et al. 2016b, JGRA, 121, 10768
Huang, S. Y., Lin, R. T., Yuan, Z. G., et al. 2021, ApJ, 922, 107
Isenberg, P. A., & Hollweg, J. V. 1983, JGR, 88, 3923
Kasper, J., Lazarus, A., Gary, S., & Szabo, A. 2003, in AIP Conf. Proc. 679, Solar Wind Ten: Proc. of the Tenth Int. Solar Wind Conf. (Melville, NY: AIP), 538
Kasper, J. C., Abiad, R., Austin, G., et al. 2016, SSRv, 204, 131
Kasper, J. C., Bale, S. D., Belcher, J. W., et al. 2019, Natur, 576, 228
Kasper, J. C., Klein, K. G., Lichko, E., et al. 2021, PhRvL, 127, 255101
Kasper, J. C., Klein, K. G., Weber, T., et al. 2017, ApJ, 849, 126
Kasper, J. C., Lazarus, A. J., & Gary, S. P. 2002, GeoRL, 29, 20
Kasper, J. C., Stevens, M. L., Korreck, K. E., et al. 2012, ApJ, 745, 162
Kasper, J. C., Stevens, M. L., Lazarus, A. J., Steinberg, J. T., & Ogilvie, K. 2007, ApJ, 660, 901
Lavraud, B., Fargette, N., Réville, V., et al. 2020, ApJL, 894, L19
Liu, M., Issautier, K., Meyer-Vernet, N., et al. 2021, A&A, 650, A14
Liu, Y. C.-M., Huang, J., Wang, C., et al. 2014, JGRA, 119, 8721
Livi, R., Larson, D. E., Kasper, J. C., et al. 2022, ApJ, 938, 138
Maneva, Y., Ofman, L., & Vinas, A. 2015, A&A, 578, A85
Marsch, E., Ao, X.-Z., & Tu, C.-Y. 2004, JGRA, 109, A04102
Marsch, E., Mühlhäuser, K.-H., Rosenbauer, H., Schwenn, R., & Neubauer, F. M. 1982, JGR, 87, 35
Maruca, B. A., & Kasper, J. C. 2013, AdSpR, 52, 723
Maruca, B. A., Kasper, J. C., & Bale, S. D. 2011, PhRvL, 107, 201101
Matteini, L., Landi, S., Hellinger, P., et al. 2007, GeoRL, 34, L20105
McManus, M. D., Verniero, J., Bale, S. D., et al. 2022, ApJ, 933, 43
Mistry, R., Eastwood, J. P., Phan, T. D., & Hietala, H. 2017, JGRA, 122, 5895
Moncuquet, M., Meyer-Vernet, N., Issautier, K., et al. 2020, ApJS, 246, 44
Mostafavi, P., Allen, R. C., McManus, M. D., et al. 2022, ApJL, 926, L38
Neugebauer, M., Goldstein, B. E., Bame, S. J., & Feldman, W. C. 1994, JGR, 99, 2505
Owens, M. 2020, Oxford Research Encyclopedia of Physics (Oxford: Oxford Univ. Press),
Peng, J., Liu, Y. C.-M., Huang, J., Klecker, B., & Wang, C. 2019, JGRA, 124, 9814

Phan, T., Dunlop, M., Paschmann, G., et al. 2004, AnGeo, 22, 2355
Phan, T., Lavraud, B., Halekas, J., et al. 2021, A&A, 650, A13
Phan, T. D., Bale, S. D., Eastwood, J. P., et al. 2020, ApJS, 246, 34
Priest, E. 2014, Magnetohydrodynamics of the Sun (Cambridge: Cambridge Univ. Press)
Pulupa, M., Bale, S. D., Bonnell, J. W., et al. 2017, JGRA, 122, 2836
Raouafi, N. E., Matteini, L., Squire, J., et al. 2023, SSRv, 219, 8
Reisenfeld, D. B., Gary, S. P., Gosling, J. T., et al. 2001, JGR, 106, 5693
Réville, V., Fargette, N., Rouillard, A., et al. 2022, A&A, 659, A110
Rouillard, A. P., Kouloumvakos, A., Vourlidas, A., et al. 2020, ApJS, 246, 37
Sapunova, O. V., Borodkova, N. L., Eselevich, V. G., Zastenker, G. N., & Yermolaev, Y. 2017, CosRe, 55, 396
Smith, E. J. 2001, JGR, 106, 15819
Stansby, D., Yeates, A., & Badman, S. 2020, JOSS, 5, 2732
Steinberg, J. T., Lazarus, A. J., Ogilvie, K. W., Lepping, R., & Byrnes, J. 1996, GeoRL, 23, 1183
Stevens, M., & Kasper, J. 2007, JGRA, 112, A05019
Suess, S. T., Ko, Y.-K., von Steiger, R., & Moore, R. L. 2009, JGRA, 114, A04103
Szabo, A., Larson, D., Whittlesey, P., et al. 2020, ApJS, 246, 47
Turner, J. M., Burlaga, L. F., Ness, N. F., & Lemaire, J. F. 1977, JGR, 82, 1921
Verniero, J. L., Larson, D. E., Livi, R., et al. 2020, ApJS, 248, 5
Wang, X., Zhao, L., Tu, C., & He, J. 2019, ApJ, 871, 204
Wang, Y., Wei, F. S., Feng, X. S., et al. 2010, PhRvL, 105, 195007
Wei, F., Feng, X., Yang, F., & Zhong, D. 2006, JGRA, 111, A03102
Wei, F., Liu, R., Fan, Q., & Feng, X. 2003, JGRA, 108, 1263
Whittlesey, P. L., Larson, D. E., Kasper, J. C., et al. 2020, ApJS, 246, 74
Winterhalter, D., Smith, E. J., Burton, M. E., Murphy, N., & McComas, D. J. 1994, JGR, 99, 6667
Yamada, M., Kulsrud, R., & Ji, H. 2010, RvMP, 82, 603
Yu, L., Huang, S., Yuan, Z., et al. 2022, JGRA, 127, e2022JA030505
Yu, L., Huang, S. Y., Yuan, Z. G., et al. 2021, ApJ, 908, 56
Yu, W., Farrugia, C. J., Lugaz, N., et al. 2014, JGRA, 119, 689
Zank, G. P., Nakanotani, M., Zhao, L.-L., Adhikari, L., & Kasper, J. 2020, ApJ, 903, 1
Zank, G. P., Zhao, L.-L., Adhikari, L., et al. 2022, ApJL, 926, L16
Zhao, L.-L., Zank, G., Hu, Q., et al. 2021, A&A, 650, A12
Zhao, L.-L., Zank, G. P., Adhikari, L., et al. 2022, ApJL, 934, L36
Zhou, Z., Wei, F., Feng, X., et al. 2018, ApJ, 863, 84
Zhou, Z., Xu, X., Zuo, P., et al. 2022, GeoRL, 49, e2021GL097564
Zhou, Z., Zuo, P., Feng, X., et al. 2019, SoPh, 294, 1
Zuo, P. B., Wei, F. S., & Feng, X. S. 2006, GeoRL, 33, L15107